Journal of Electroceramics, 14, 5–23, 2005

Interface Defect Chemistry and Effective Conductivity in Polycrystalline Cerium Oxide

ANDREAS TSCHÖPE*
Universität des Saarlandes, Gebäude 43B, Postfach 151150, 66041 Saarbücken, Germany

Submitted December 8, 2003; Revised May 11, 2004; Accepted June 14, 2004

Abstract. Polycrystalline cerium oxide exhibits increasing electronic and decreasing ionic conductivity upon reduction of the grain size. In the present study, the origin of this effect was examined. Temperature-programmed reduction (TPR) and oxygen titration measurements on nanocrystalline cerium oxide revealed a large excess oxygen deficiency associated with the surface. Using a two-phase model for the combined system of the bulk phase in equilibrium with a surface layer, this enhanced oxygen deficiency could be explained by a reduced binding energy of surface oxygen ions in agreement with results from atomistic computer simulations. The model also revealed that this segregation of oxygen vacancies is the origin of an intrinsic space charge potential. Translating this effect to polycrystalline cerium oxide and taking into account the segregation of dopants and the accumulation/depletion of charge carriers, it was possible to model the grain size dependence of electrical conductivity and thermopower of polycrystalline cerium oxide. A straightforward 1-dimensional numerical model and a change from Boltzmann to Fermi-Dirac statistics allowed to calculate the conductivity of heavily doped polycrystalline cerium oxide for grain sizes in the range of 5–10,000 nm and acceptor concentrations up to 20%. Using this approximation, the effect of grain size on mixed ionic/electronic conductivity and the electrolytic domain boundary was investigated.

Keywords: CeO_2, defect chemistry, oxygen deficiency, grain boundary, space charge

1. Introduction

In technical applications, electroceramic materials are usually employed in polycrystalline form rather than as single crystals. Hence, their physical properties are often influenced if not even determined by the grain boundaries, which are inevitably present in polycrystalline materials [1–3]. The grain size of a material—and as a consequence the grain boundary density—is strongly influenced by materials processing. Therefore, if the specific effect of grain boundaries is known, particular properties may be tailored through the microstructure of the material. Whether material processing should be aiming at a fine or coarse-grained microstructure depends on whether grain boundaries are advantageous or detrimental with respect to the desired properties. The present report focusses on the grain boundary effect in polycrystalline cerium oxide,

*E-mail: antsch@rz.uni-sb.de

which is a mixed ionic/electronic conductor (MIEC) and which has been intensively investigated as base material for solid electrolytes.

The physical properties and the underlying defect chemistry of the cerium oxide bulk phase are well understood and documented in numerous experimental studies on single crystals, or coarse grained polycrystalline materials in which the bulk and grain boundary contributions could be separated [4–6]. Cerium oxide, when doped with lower-valent cations, exhibits high ionic conductivity due to extrinsic oxygen vacancies, which are generated for charge compensation. On the other hand, the loss of oxygen to the gas phase results in an increasing electronic conductivity. While the mixing of electronic and ionic conductivity may be desirable for certain applications (e.g. oxygen membranes, electrodes) the use of cerium oxide as solid electrolyte requires that the ionic partial conductivity surmounts the electronic contribution (electrolytic domain) [7]. It is also well known that—depending on the nature of the dopant—the formation of dopant/oxygen vacancy associates results in a reduction of ionic conductivity [8–10]. The strength of association is related to the size mismatch of the dopant and is minimized for Gadolinium, so that Gd-doped cerium oxide (CGO) is currently the most frequently studied ceria-based oxygen ion conductor [11–14].

In contrast to the bulk phase, there is not yet a general agreement on the impact of grain boundaries to the overall electrical conductivity. Apparently, the grain boundary effect is the superposition of at least three different contributions, which will be briefly outlined in the following.

A first particular grain boundary effect in polycrystalline cerium oxide, indicated by a significant decrease in ionic conductivity [15], was shown to be due to thin layers of an insulating siliceous phase along the grain boundaries [16]. This blocking effect of grain boundaries could be nearly eliminated by using ceria ceramics of high purity (low Si content) [17]. Alternatively, this problem could be overcome by changing to a polycrystalline ceramic with a very small grain size. It has been demonstrated for nanocrystalline YSZ that the resistance per grain boundary decreased for smaller grain sizes as the impurities were spread over a large grain boundary area and could not form a continuous insulating layer [18].

A series of studies on nanocrystalline cerium oxide ceramics revealed a second grain boundary effect on the electrical conductivity. The most important experimental observation was an increasing electronic conductivity as the grain size was reduced [19–26]. An analysis, based on the point defect chemistry of bulk cerium oxide, suggested that this increase was due to an enhanced oxygen deficiency which was attributed to the grain boundaries in the nanocrystalline materials. The assumption of an enhanced oxygen deficiency was supported by a reduced apparent activation energy of electronic conductivity, which suggested a reduced enthalpy of reduction for the nanocrystalline cerium oxide [19, 21–23]. The same experimental results were also analyzed in terms of a model that was based on the existence of space charge layers along grain boundaries [25–27]. This space charge model was originally used to describe the conductivity enhancement of heterogeneous mixtures of silver halides with insulating alumina [28] and later applied to a variety of heterogeneous and single-phase ionic materials [26, 29–33]. When applied to polycrystalline cerium oxide, the enhancement and grain size dependence of electronic conductivity [26, 27] as well the grain size dependence of thermopower [34] could be consistently explained by the presence of space charge layers with a positive space charge potential of 0.3–0.7 V.

A third possible contribution of grain boundaries to electrical conductivity is due to segregation of solute ions, i.e., the accumulation of solute ions in the structural core and/or the vicinity of grain boundaries. The bulk concentration of dopants, which are introduced to the material in order to increase the extrinsic ionic conductivity, is reduced to the extent at which the dopants accumulate at the grain boundaries. This indirect impact of grain boundaries on bulk properties is significant for large segregation ratios and materials with large specific grain boundary area, i.e. small grain size. The segregation ratio depends on the dominating driving force (e.g. elastic strain energy, electrostatic energy) which is determined by the properties of the cerium oxide host matrix and the specific nature of the dopant. We note that segregation may be suppressed if materials processing resulted in a non-equilibrium distribution of solute ions (e.g. Mott-Schottky model).

The present report is aiming at a detailed analysis of the latter two contributions which become significant when high-purity and/or fine grained materials are employed. It is the primary intention of this report to show, that the original idea of an enhanced oxygen deficiency at grain boundaries as the origin of enhanced electronic conductivity in nanocrystalline cerium oxide

is consistent with the space charge model. As a matter of fact, if grain boundaries exhibit an excess oxygen deficiency, a space charge potential will generally be established as a result of thermodynamic equilibrium with the bulk crystallites. An important step towards this objective is to gather complementary experimental evidence for the excess oxygen deficiency associated with grain boundaries or—more generally—interfaces in cerium oxide.

Besides its prominent role in solid state ionics, cerium oxide has been intensively investigated for application in heterogeneous catalysis at which the propensity of ceria to exchange oxygen with the surrounding gas phase plays an important role. A comprehensive review of the catalytic properties of ceria-based materials can be found in ref. [35]. In the redox mechanism of catalytic oxidation reactions, the surface of the oxide catalyst is continuously reduced (e.g. by CO or hydrocarbons) and re-oxidized by oxygen [36]. The well-known application of cerium oxide in the 3-way catalytic converter is partially based on the cyclic release and storage of oxygen, which buffers the oscillations in the composition of the fuel/air mixture thus improving the converter efficacy [37–39]. Methods for the characterization of catalytic properties, in particular those that focus on surface reduction, could provide additional insight into the defect chemistry of nanocrystalline materials. The approach taken in this study can be outlined as follows. A brief summary of the defect chemistry of the cerium oxide bulk phase, which serves as reference state, is the starting point of the present analysis. Macroscopic properties of surfaces/interfaces will be characterized in the Gibbsian framework. In particular, the Gibbsian excess oxygen deficiency of cerium oxide surfaces will be examined and quantified using results from temperature-programmed reduction (TPR) and oxygen titration measurements. These experimental results will be analyzed by a point defect model, in which the interface (surface) is treated as a thin layer of a second phase with different defect formation energies as compared to the bulk phase [40]. This two-phase model, which is first applied to an individual interface in equilibrium with the bulk will then be tranfered to crystals of finite size in order to introduce the grain size as a variable. This final step enables to model effective properties (partial conductivities, thermopower) of a polycrystalline material as function of grain size. As noticed above, a particular aspect associated with grain size is the segregation of acceptor ions, which are introduced into cerium oxide to enhance ionic conductivity. Depending on the dominating segregation mechanism (driving force), different scaling-laws for the grain size dependence of the effective conductivities are obtained. The analysis further allows to predict the consequences of the intrinsic grain boundary effect on mixed ionic/electronic conductivity and the electrolytic domain of polycrystalline cerium oxide.

2. Volume Phase Defect Chemistry

The equilibrium concentrations of point defects in cerium oxide can be calculated using the formalism of defect thermodynamics [6]. The laws of mass action for the dominant ionic disorder (Anion-Frenkel equilibrium) and the electronic disorder (electron-hole formation) are combined with the charge neutrality equation (valid in the volume phase only) to obtain the concentrations of doubly ionized oxygen vacancies $[V_{\mathrm{O}}^{\cdot\cdot}]$, oxygen interstitial ions $[\mathrm{O}_i^{''}]$, electrons n and holes p (in principle, further defects such as neutral or singly ionized oxygen vacancies could be introduced but are excluded in the present study). It has been demonstrated, that the concentrations of holes and oxygen interstitials in cerium oxide are negligible compared to electrons and oxygen vacancies in the regime of oxygen partial pressures below $p_{\mathrm{O}_2}/p^\circ = 1$ ($p^\circ = 1.013{\cdot}10^5$ Pa) [6]. Hence, it is then sufficient to consider the external equilibrium, i.e. the exchange of oxygen between the solid oxide and the gas phase,

$$\mathrm{O}_{\mathrm{O}}^{x} \rightleftharpoons V_{\mathrm{O}}^{\cdot\cdot} + 2e' + \frac{1}{2}\mathrm{O}_2 \tag{1}$$

with the corresponding law of mass action

$$\frac{[V_{\mathrm{O}}^{\cdot\cdot}]n^2 p_{\mathrm{O}_2}^{1/2}}{[\mathrm{O}_{\mathrm{O}}^{x}]} = K_R^0(T) = K_R^0 \exp\left(-\frac{H_R}{k_B T}\right). \tag{2}$$

The material constants were taken from ref. [41] as $K_R^0 = 3.73 \cdot 10^6$ atm$^{-1/2}$ [42] and $H_R = 4.67$ eV . In the charge neutrality equation,

$$n + [A'_{\mathrm{Ce}}] = 2[V_{\mathrm{O}}^{\cdot\cdot}], \tag{3}$$

trivalent acceptor impurities $\mathrm{A}'_{\mathrm{Ce}}$ are included in addition to oxygen vacancies and electrons, because a certain concentration of such lower-valent cations is present in any real material or may be introduced

purposely in order to increase the ionic conductivity. The concentrations of penta- or hexa-valent donors are neglected, since corresponding elements are rarely present in significant amounts.

A straightforward procedure to calculate the defect concentrations was suggested by Porat and Tuller [43]. All defect concentrations in the charge neutrality equation are expressed in terms of n, p_{O_2}, and the appropriate equilibrium constants. The function to be solved in our case is given by

$$p_{O_2}(n) = \left(\frac{2K_R(T)}{n^2(n + [A'_{Ce}])} \right)^2. \quad (4)$$

Equations (3) and (4) allow to calculate the volume concentrations n_0 and $[V_O^{\cdot\cdot}]_0$ for a given temperature, oxygen partial pressure and acceptor concentration.

A possible and indirect experimental access to the defect concentrations is provided by measurements of electrical conductivity. The concentrations and the mobilities of electrons and oxygen vacancies determine the electronic and ionic partial conductivities of single crystalline cerium oxide, respectively. In this study, the electron mobility was taken from ref. [6] as

$$\mu_e(T) = \frac{3.9 \cdot 10^2 \ \frac{cm^2 K}{Vs}}{T} \exp\left(-\frac{0.4 \text{ eV}}{k_B T} \right). \quad (5)$$

The effective mobility of oxygen vacancies was derived by an analysis of experimental data on microcrystalline cerium oxide as [24]

$$\mu V_O^{\cdot\cdot}(T) = \frac{1.5 \cdot 10^2 \frac{cm^2 K}{Vs}}{T} \exp\left(-\frac{0.71 \text{ eV}}{k_B T} \right). \quad (6)$$

From the volume concentrations and mobilities of charge carriers, the partial ionic and electronic conductivities can be calculated for given temperature and oxygen partial pressure as function of acceptor concentration (see Fig. 1). The dependence of the partial conductivities from the acceptor concentration can be divided into two regions; (i) low acceptor concentrations, at which the conductivities are nearly independent of $[A'_{Ce}]$ and $\sigma_{el} \gg \sigma_{ion}$, and (ii) high acceptor concentrations, at which the ionic conductivity increases proportional to $[A'_{Ce}]$ while the electronic conductivity decreases $\propto [A'_{Ce}]^{0.5}$. A characteristic feature of cerium oxide is the transition from predominantly electronic to ionic conductivity which occurs at an intermediate acceptor concentration of roughly 1 ppm at $T = 500°C$

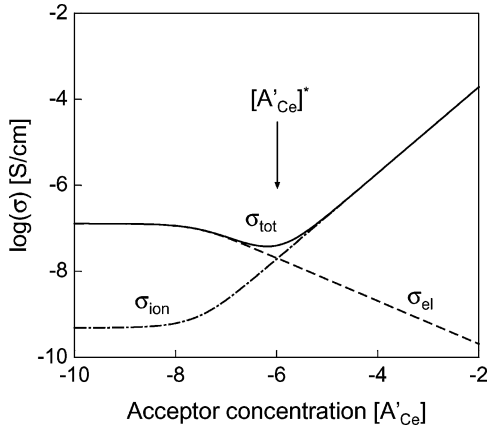

Fig. 1. Ionic, electronic and total electrical conductivity of the cerium oxide volume phase at $T = 500°C$ and $p_{O_2}/p^0 = 0.21$ as function of acceptor concentration (molar fraction). The cross-over from predominantly electronic to ionic conductivity is marked by the arrow.

and $p_{O_2}/p^0 = 0.21$. This cross-over represents the minimum acceptor concentration, necessary for predominantly ionic conductivity and defines the borderline of the electrolytic domain of the volume phase. The electrolytic domain is also limited by temperature and oxygen partial pressure. As shown in Fig. 2, the ionic/electronic domain boundary may be crossed by temperature increase or decrease in oxygen partial pressures. Within limits, the domain border can be shifted—and hence the cross-over deferred—by increasing the acceptor concentration [7, 12, 44].

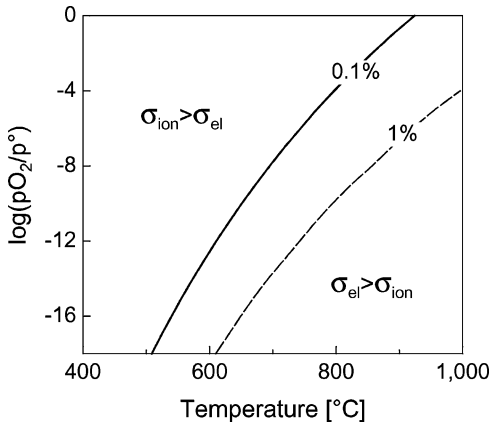

Fig. 2. Boundary between the ionic and electronic domain as function of T and p_{O_2}/p^0 for two different acceptor concentrations of 0.1 and 1%.

The defect chemistry of acceptor-doped cerium oxide, as outlined above, is a first approximation since further effects, e.g. the impact of point defect association, were not considered. In the following, this model for the homogeneous phase with infinite spatial extent will serve as reference state for the analysis of the contribution of interfaces.

3. Interfaces and Excess Oxygen Deficiency

A description of macroscopic thermodynamic quantities in systems, that contain interfaces, was developed by Gibbs [45]. In this approach, the total excess of an extensive macroscopic quantity χ_i, defined as

$$\Delta\chi_i = \chi_i^I - \chi_i^0, \tag{7}$$

is introduced, where χ_i^I and χ_i^0 denote the values of χ_i in a system with and without interface, respectively (see also [46, 47]). When the total excess is divided by the interface area A of the system, the specific excess is obtained,

$$\{\chi_i\} = \frac{\chi_i^I - \chi_i^0}{A}. \tag{8}$$

A prominent example is the specific excess in the Gibbs free energy of a polycrystalline material, which defines the grain boundary free energy and represents the driving force for grain growth (at very small grain sizes, the contribution of triple lines to the excess Gibbs free energy may become significant too). More important in the context of this study is the excess oxygen deficiency or—in other words—the excess concentration of oxygen vacancies,

$$\Delta[V_O^{\cdot\cdot}] = [V_O^{\cdot\cdot}]^I - [V_O^{\cdot\cdot}]^0. \tag{9}$$

In the following, the excess oxygen deficiency associated with surfaces of cerium oxide will be examined. An approximate value for this excess of oxygen vacancies can be obtained experimentally. For instance, the oxygen loss of metal oxide nanoparticles during reduction can be quantified by temperature-programmed reduction measurements, a technique that is commonly used for the characterization of metal oxide catalysts [48]. The material is initially in an oxidized state and exposed to a flow of reducing gas at low temperature. If this initial temperature is low enough, the reduction is prevented by the activation energy of the chemical reaction so that the sample and the gas phase are held in a kinetically stabilized non-equilibrium state. When the temperature is increased, thermal activation initiates the reduction process. By chemical gas analysis of the effluent gas and mass balance, the amount of extracted oxygen can be determined. A typical H_2—TPR spectrum of nanocrystalline cerium oxide is shown in Fig. 3. The reduction proceeds in two steps. A first reduction peak, starting at 350°C with a peak maximum at 500°C, is followed by a second increase in the rate of reduction above 600°C [49]. The origin of the first reduction reaction can be revealed by the following analysis. It may be assumed that the reduction associated with this peak is the superposition of bulk reduction and an excess contribution due to the surface of the nanoparticles. Then, the total amount of hydrogen consumption should be the sum of two terms, one being proportional to the sample mass m_S while the other is proportional to the surface area A_S of the sample,

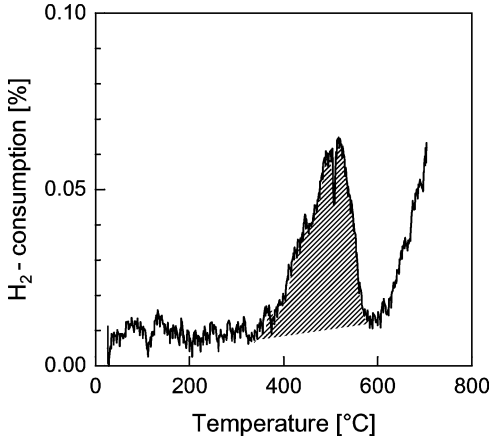

Fig. 3. Hydrogen consumption during temperature-programmed reduction of nanocrystalline cerium oxide. The integrated peak area (hatched) is further analyzed as function of specific surface area [49].

$$N_{H_2}^{tot} = p_1 m_S + p_2 A_S, \tag{10}$$

with constants p_1 and p_2, respectively. When divided by the sample mass, the specific hydrogen consumption is obtained,

$$\frac{N_{H_2}^{tot}}{m_S} = p_1 + p_2 \frac{A_S}{m_S}, \tag{11}$$

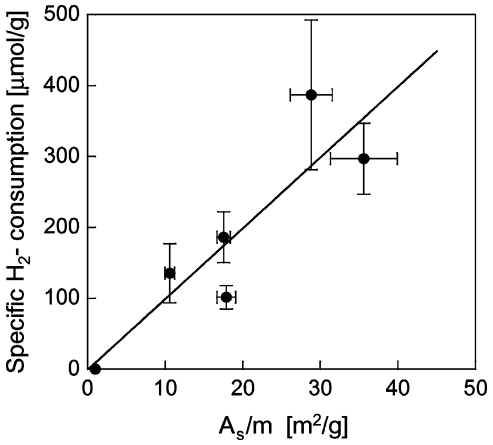

Fig. 4. Specific hydrogen consumption during temperature-programmed reduction of nanocrystalline cerium oxide as function of specific surface area. The slope of the linear fit provides the specific excess of oxygen vacancies [49].

with a linear relationship with respect to the specific surface area A_S/m_S. By analysis of TPR-measurements on samples with varying specific surface area, the values $p_1 = 10.2 \pm 6.8$ μmol/g and $p_2 = 9.6 \pm 1.4$ μmol/m^2 were determined, Fig. 4 [49]. If we assume that each hydrogen molecule has reacted with one oxygen atom to water (as confirmed by mass spectroscopy) and that the oxygen deficiency in the initial state was negligible, the value of p_2 represents the specific excess oxygen deficiency after reduction in hydrogen at 600°C. We note that for $A_S/m_S > 10$ m^2, this excess is one order of magnitude larger than the bulk oxygen deficiency p_1. The second increase in the hydrogen consumption above 600°C is independent of the surface area and is therefore associated with further reduction of the bulk material. These results provide unequivocal evidence for a significant specific excess oxygen deficiency associated with surfaces in cerium oxide. The value of 9.6 μmol/m^2 may be compared with the number of CeO_2 formula units per unit surface area to estimate the surface stoichiometry after reduction. As this number depends on the crystallography of the surface, only average values are available. For instance, a value of 7.97 μmol/m^2 was estimated by Bernal et al. [50] which implies that a surface composition of roughly $CeO_{0.8}$ was achieved during H_2—TPR. A similar enhanced reduction was observed in ceria based nanocrystalline porous materials using photoelectron spectroscopy measurements, combined with *in situ* oxidation-reduction treatments [51], or thermogravimetric analysis [52].

A major drawback of the TPR-measurements is the non-equilibrium condition with respect to the oxygen chemical potential. In order to characterize the excess oxygen deficiency of the interfaces in equilibrium with the gas phase, isothermal titration measurements have been performed. The first study on nanocrystalline cerium oxide by coulometric titration was reported by Porat et al. [53]. In the range of oxygen partial pressures between 10^{-1} and 10^{-4} a significantly larger oxygen deficiency (CeO_{2-x}) was observed as compared to coarse-grained reference samples in combination with an unusual power-law dependence $x \propto p_{O_2}^{-1/2}$. For low oxygen partial pressures, the oxygen deficiency could be characterized by volumetric titration of hydrogen-reduced nanocrystalline cerium oxide [54]. A series of fixed volume doses of oxygen was injected into a sample compartment of known volume, which contained a hydrogen-reduced specimen. The equilibration of oxygen chemical potential was monitored by a potentiometric oxygen sensor. The injections were repeated until the oxygen uptake by the sample, calculated from the mass balance, vanished. The measured quantities allowed to calculate the specific excess oxygen vacancy concentration as function of oxygen partial pressure for the given temperature during the isothermal measurement, Fig. 5. The maximum excess oxygen vacancy concentration was found to be 6 μmol/m^2 at 500°C

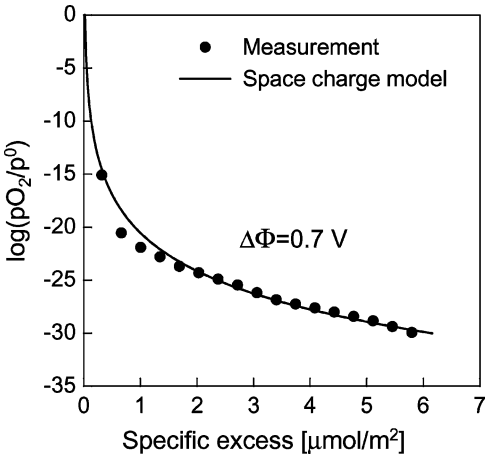

Fig. 5. Relationship between equilibrium oxygen partial pressure and specific surface excess oxygen deficiency, measured by volumetric titration at $T = 500$°C. The analysis based on the space charge model yielded a space charge potential of 0.7 V.

and an effective oxygen partial pressure of 10^{-27} atm. From these measurements, a relationship between defect concentrations and thermodynamic state variables becomes available which can be analyzed in terms of a thermodynamic defect model.

As a first conclusion, TPR- and oxygen titration measurements on nanocrystalline cerium oxide confirm a significant excess oxygen deficiency associated with the surface. It is reasonable to connect the surface excess oxygen deficiency with a reduced binding energy of the surface oxygen ions. However, it should be pointed out that the mere fact of a lower temperature for the surface reduction peak in TPR as compared to bulk reduction is not necessarily a proof for such a reduced binding energy. Rather, the peak temperature is determined by the activation energy of the chemical reaction. By variation of the heating rate, this activation energy can be derived from the peak temperature shift and values of 0.6–1.0 eV were obtained from CO-TPR and H_2—TPR [55].

Regarding grain boundaries in polycrystalline cerium oxide, an enhanced oxygen deficiency was also recently revealed by chemical analysis using EELS measurements [56]. While the excess oxygen deficiency appears to be a common characteristic for both surfaces and grain boundaries in cerium oxide, quantitative differences may be expected due to different degrees of unsaturation in the atomic coordination [57]. In the following chapter, the effect of a reduced binding energy for oxygen ions—i.e. a reduced energy of oxygen vacancy formation—at surfaces or grain boundaries on the overall defect equilibrium will be investigated using the model suggested by Jamnik et al. [40]. Furthermore, it will be shown how the segregation of acceptor ions can be included in the modelling of interface defect chemistry.

4. Defect Chemistry of Interfaces

4.1. Undoped Cerium Oxide

In the defect chemistry as introduced in Section (2.1), the condition of local charge neutrality, Eq. (3), is a fundamental ingredient associated with the symmetry of the crystalline volume phase. In the remaining part of this study, this condition is abandoned and replaced by the Poisson-Boltzmann or Poisson-Fermi-Dirac equation. This generalization is required because of the broken symmetry of finite crystallites or polycrstalline materials. This approach is only briefly outlined as it has been described in numerous publications [29, 40, 58–61].

In ionic materials, point defects generally carry a net electric charge $q_i = z_i e_0$ relative to the perfect lattice, so that the contribution of Coulomb energy to the total energy of defect formation must be taken into account, and

$$x_i = X_i \exp\left(-\frac{g_i^0 + z_i e_0 \Phi}{k_B T}\right), \tag{12}$$

where x_i denotes the molar fraction of the point defect, X_i the molar fraction of potential defect sites in the crystal lattice [62] and Φ the electrical potential at the defect site with respect to a reference point. Commonly chosen reference points are extended defects, such as surfaces, grain boundaries or step dislocations, which serve as source or sink for point defects. In equilibrium and for low defect concentrations (dilute limit), minimization of the overall Gibbs free energy results in a potential distribution, which is determined by the Poisson-Boltzmann equation,

$$\nabla^2 \Phi(\vec{r}) = -\frac{c_0 \Gamma}{\epsilon \epsilon_0} \sum_i z_i C_i \exp\left(-\frac{g_i^0(\vec{r}) + z_i e_0 \Phi(\vec{r})}{k_B T}\right), \tag{13}$$

with the volume density of formula units $\Gamma = \rho N_A / M$ where ρ is the density and M the molar mass of the ionic solid and N_A is Avogardos constant. It was argued by Frenkel [58] and further analyzed by Kliewer and Koehler [60] that a difference in the formation energies g_i^0 of the various point defects in an ionic solid is already the origin of a space charge potential between the bulk phase and the reference point, with respect to which the formation energies are defined. The asymmetry in the formation energy is balanced by the Coulomb energy term associated with the crossing of the space charge potential. This model has been criticized for the assumption that the reference point is a perfect source and sink for point defects with infinite capacity and vanishing layer thickness. For instance, the obvious structural differences between surface, grain boundaries and step dislocations are completely neglected. A more general model was introduced by Jamnik et al. [40], in which the interface is treated as a second phase with a finite number of lattice-like sites and a finite

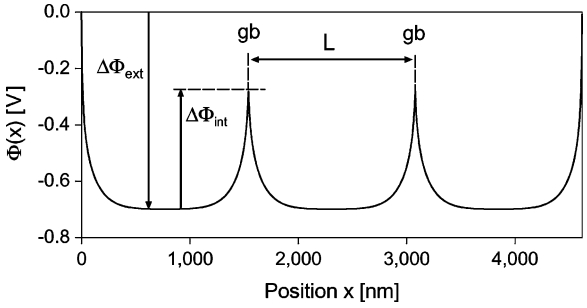

Fig. 6. Electrical potential profile across a stack of three crystalline layers with two external and two internal interfaces. Notice, that the surface is the reference point for $\Delta\Phi_{ext}$ whereas $\Delta\Phi_{int}$ is related to the potential in the bulk phase.

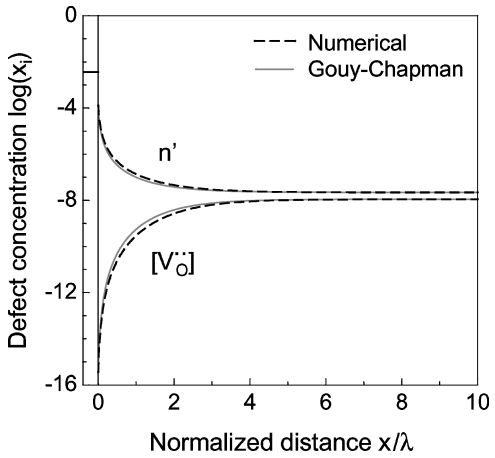

Fig. 7. Concentration of electrons and oxygen vacancies as function of normalized distance from an interface for $T = 500°C$, $p_{O_2}/p^0 = 0.21$ and $\Delta\Phi = 0.54$ V. Comparison of numerical results and analytical approximation.

layer thickness. In fact, EXAFS measurements on various nanocrystalline metal oxides suggest that atoms at grain boundaries essentially occupy lattice sites of either one of the crystallites that meet at the grain boundary [63]. The specific nature of the interface is taken into account by different values for the defect formation energies g_i^0 as compared to the bulk crystallites. The solution of the Poisson-Boltzmann equation with a local variation of the quantities g_i^0 provides the equilibrium distribution of the electrical potential, as shown in Fig. 6 for the example of a stack of three crystalline layers with two external boundaries and two internal interfaces. The space charge potential at the external boundaries $\Delta\Phi_{ex}$ is determined by the asymmetry in the formation energies g_n^0 and $g_{V_O^{\cdot\cdot}}^0$ as argued by Frenkel, Kliewer and Koehler. The potential $\Delta\Phi_{int}$ at the internal interfaces is the result of a difference Δg_i^0 in the defect formation energy for the same defect (electrons, oxygen vacancies, or both) between the interface layer and the bulk. At this point, we would like to notice that $\Delta\Phi_{int}$ is intrinsic in the sense, that it is a property of pure cerium oxide, even in the absence of impurity ions. The two space charge potentials are independent in so far as $\Delta\Phi_{int}$ is a function of the Δg_i^0 but independent of the absolute values g_i^0. This is rather important, since the absolute values for g_i^0—and hence $\Delta\Phi_{ex}$—are usually unknown. The only information that may be available is the equilibrium constant of the corresponding point defect reaction, which is basically the sum of the g_i^0. If the equilibrium constant is arbitrarily split into the various contributions g_i^0, the external potential $\Delta\Phi_{ex}$ is completely determined. However, the internal potential $\Delta\Phi_{int}$ is unaffected by this arbitrary separation but depends on the differences Δg_i^0 only. It should be noticed that the trilayer topology is chosen for practical reasons only in order to mask out the effect of the external potential in the calculation. The *internal* interface does not necessarily represent grain boundaries only, as may be suggested by the topology, but could also be applied to model the explicit defect chemistry of surfaces (as an alternative to the *ideal* surface in the Frenkel model).

After numerical solution of the Poisson-Boltzmann equation, the obtained potential distribution and Eq. (12) allow the calculation of the defect concentration profiles. An example for the space charge potential as function of distance from the internal interface is shown in Fig. 7. In this particular example, a difference in the energy of oxygen vacancy formation $\Delta g_{V_O^{\cdot\cdot}}^0 = -1.9$ eV between the interface and the bulk phase was assumed, resulting in a space charge potential of $\Delta\Phi_{int} = 0.54$ V.

In the analysis of space charge effects, the space charge potential $\Delta\Phi$ is usually handled as an empirical variable. In fact, if $\Delta\Phi$ is known, the potential and concentration profiles can also be straightforwardly described by the Gouy-Chapman theory for charged interfaces in liquid electrolytes [64, 65]. The electrical potential at a distance ξ from the planar boundary is given by the analytic expression [66]

$$\Phi(\xi) = \frac{2k_BT}{ze_0} \ln\left(\frac{1+\Theta\exp(-\xi/\lambda)}{1-\Theta\exp(-\xi/\lambda)}\right), \qquad (14)$$

with two characteristic parameters, the screening length

$$\lambda = \left(\frac{\epsilon\epsilon_0 k_B T}{\sum_i (z_i e_0)^2 x_{i0} \Gamma} \right)^{1/2} \tag{15}$$

and a profile parameter

$$\Theta = \tanh\left(\frac{z e_0 \Delta\Phi}{4 K_B T} \right), \tag{16}$$

which is determined by the space charge potential $\Delta\Phi$ (The Gouy-Chapman profiles are applicable to both $\Delta\Phi_{ex}$ and $\Delta\Phi_{int}$). The concentration profiles are obtained by combining Eqs. (12) and (14) to

$$\frac{x_i(\xi/\lambda)}{x_{i0}} = \left(\frac{1 + \Theta \exp(-\xi/\lambda)}{1 - \Theta \exp(-\xi/\lambda)} \right)^2. \tag{17}$$

The Gouy-Chapman model is based on the assumptions that the defect concentrations are low, the electrolyte is symmetric (i.e. $|z_i| = \text{const.}$), and the screening length λ is much smaller than the dimension L of the electrolyte volume. Obviously, the numerical solution of the Poisson-Boltzmann equation is identical to the Gouy-Chapman profile if these conditions are met. However, the analytical model provides only an approximation of $\phi(\xi)$ when the electrolyte is not symmetric as it is the case for cerium oxide. The approximation is usually acceptable, if the space charge effect is strong. In this case, the local charge density and hence the space charge potential profile is mainly determined by those point defects, which exhibit the highest concentrations and which are accumulated in the space charge layer, whereas depleted point defects do not significantly contribute to the charge density. For cerium oxide with positive space charge potential, the profile parameter Θ and the potential profile $\Delta\Phi(\xi)$ are determined by the concentration of electrons or acceptor ions, i.e. $z_1 = -1$, and the corresponding concentration profiles can be obtained from Eq. (17). The concentration profile for oxygen vacancies follows the same potential profile but with a different charge $z_2 = 2$ in Eq. (12). A comparison with the numerical result reveals, that for the asymmetric electrolyte the screening length λ is underestimated by the Gouy-Chapman model. It turns out that an excellent agreement with the numerical potential profile is obtained, when a modified screening length $\lambda^* = \sqrt{3/2} \cdot \lambda$ is used. Although this modified Gouy-Chapman profile is still an approximation only, one may take advantage of the straightforward analytical approach towards the analysis of experimental results. While λ is completely determined by the bulk defect concentrations, the space charge potential, which determines the second parameter Θ of the Gouy-Chapman model, is unknown so far. As discussed above, the space charge potential $\Delta\Phi_{int}$ depends on the differences in defect formation enthalpies. As shown in Appendix A, an approximate relationship between the space charge potential and the difference in the formation energies for oxygen vacancies can be derived (under the assumption that $\Delta\phi_{int}$ is dominated by $\Delta g^0_{V_O^{\cdot\cdot}}$) as

$$\Delta\Phi_{int} \approx -\frac{2}{5}\left[k_B T \ln(2\lambda * \Gamma^{1/3}) + \Delta g^0_{V_O^{\cdot\cdot}} \right]. \tag{18}$$

The Gouy-Chapman approximation for the space charge model can now be employed for a quantitative analysis of the oxygen titration measurements on nanocrystalline cerium oxide. By comparison with the experimental results, the space charge potential of the cerium oxide surfaces and the corresponding difference in the enthalpy of oxygen vacancy formation will be determined. For comparison, space charge potentials will be calculated numerically, based on defect formation energies for cerium oxide surfaces, which were derived from atomistic computer simulations and reported in the literature.

For large effects ($\Theta \approx -1$) the excess charge in the space charge layer is dominated by the accumulated electrons. Integration of the electron density across the space charge layer yields the specific excess [27],

$$\{n\} = -4 \frac{\lambda^* \Theta}{1 + \Theta} \cdot n_{bulk}. \tag{19}$$

If we assume that the excess oxygen vacancies at the surface provide the counter charge to the space charge layer, the specific excess $\{[V_O^{\cdot\cdot}]\}_{surf} = 0.5\{n\}_{scl}$ is obtained. The bulk defect concentrations and Eqs. (15), (16) and (19) then allow to calculate the specific excess oxygen vacancy concentration as function of T, p_{O_2}/p^0, $[A'_{Ce}]$ and $\Delta\Phi$. A fit of this model to the experimental results obtained by oxygen titration measurements is shown in Fig. 5 and yielded a space charge potential of $\Delta\Phi = 0.7$ V. With Eq. (30) (see Appendix A) this value translates to a difference in the energy of oxygen vacancy formation of $\Delta g^0_{V_O^{\cdot\cdot}} \approx$

−2.3 eV for the surface. This value may be compared with results obtained from computer simulations.

The enthalpy of the oxygen exchange equilibrium at cerium oxide surfaces has been calculated by atomistic computer simulation [67–70]. For all investigated crystallographic orientations, this enthalpy was found to be smaller as compared to the bulk value, which implies that the surfaces are more reduced than the bulk phase. According to the study by Balducci et al., the lower enthalpy is limited to the first 1–2 crystalline layers only [70]. Calculated differences in ΔH_R were ranging form −3.87 eV for (111), −7.05 eV for (110) to −12.83 eV for the (310) surface [67, 68] and similar but slightly smaller values were reported by Conesa [69]. It should be noticed that this quantity has two characteristic contributions; the differences in (i) the energy for oxygen vacancy formation, and (ii) the energy to substitute Ce^{4+} by Ce^{3+} between the surface and the bulk. Both components are independent and represent the segregation energies for oxygen vacancies and electrons, respectively. The net charge at the interface is then depending on the balance between vacancy and electron segregation. If both defects segregate simultaneously and proportional, the surface remains neutral. However, at large segregation enthalpies for both defects, the surface of cerium oxide will always possess a positive excess charge, provided the oxygen vacancies are fully ionized and cerium is not reduced to oxidation states below Ce^{3+}. In the most extreme case, a stoichiometry of $Ce^{3+}O_0^{-2}$ would be reached at the interface. Based on the segregation energies obtained from ref. [68], the space charge potentials were calculated for the various surfaces (Table 1). Even though the segregation enthalpies for electrons are larger as compared to vacancies, the latter dominate the excess charge at the interface and hence the space charge potential. Only for the most stable (111) surface, a negative space charge potential is expected. Recent measurements of the electronic structure of cerium oxide (111) surfaces by photoelectron spectroscopy (UPS) revealed a band bending with increasing $E_V - E_F$, which suggested the existence of a surface dipole with positive excess charge in the interface and a negative space charge layer [71]. The apparent contradiction with the expected negative surface charge may be due to the non-equilibrium conditions during UPS measurements in ultrahigh vacuum.

Table 1. Space charge potential at various surfaces, obtained by numerical solution of the Poisson-Boltzmann equation, using defect formation energies from ref. [68].

Surface	$\Delta g^0_{V_O^{\cdot\cdot}}$ (eV)	Δg^0_n (eV)	$\Delta\Phi_{\text{int}}$ (V)
(111)	−0.4	−1.73	−0.39
(110)	−1.5	−2.78	0.15
(310)	−2.47	−5.18	0.64

A comparison of the space charge potential $\Delta\Phi = 0.7$ V obtained from the analysis of the oxygen titration measurement with the values given in Table 1 reveals a good agreement with the computer simulation of the (310) surface, i.e. the surface with the lowest symmetry, but significant differences with respect to the values for the two most stable surface structures. It is important to notice, that special surfaces, which were investigated in the computer simulation, are not necessarily representative for the surfaces of nanocrystalline particles. Furthermore, the experimental studies were performed on large ensembles of crystallites so that only average properties were measured. This situation is comparable to the grain boundary excess free energy, which is also known to depend on the particular crystallography. Coincidence grain boundaries with high symmetry exhibit particularly small excess free energies as compared to general grain boundaries. The measured average value for a given polycrystalline sample is determined by the crystallite orientation distribution function (ODF) and the grain boundary misorientation distribution function (BMD) [72]. If the sample is homogeneous and isotropic in both distribution functions, the macroscopic average value is well defined but can be significantly different from the values for the special boundaries. With respect to the present study, it may therefore not be surprising that the average value for the space charge potential, obtained from the analysis of the titration measurement, is larger than the individual values for the two most stable surfaces.

In the present analysis, only fully ionized oxygen vacancies are taken into account while the contribution of singly ionized or neutral oxygen vacancies as well as adsorbed oxygen was neglected. Porat et al. observed an unusual power-law dependence of the oxygen uptake of nanocrystalline cerium oxide during titration measurements with an exponent −1/2 [43]. Two alternative explanations for this behavior were discussed. The results could be explained by lower ionization states of oxygen vacancies but also by the adsorption of oxygen on the cerium oxide surface. In fact, ionosorption of oxygen on metal oxide surfaces, involving various species of different ionization and

dissociation (O_2^-, O_2^{2-}, O^-) are a well established [36]. It can be assumed that the contribution of adsorption phenomena to titration measurements may be larger at the high oxygen partial pressures, employed by Porat, as compared to the very low partial pressures, used in the present study. In a recent thermogravimetric study, Kim et al. analyzed the partial pressure dependence of oxygen stoichiometry and suggested that a significant fraction of oxygen was present in lower ionization states [73]. However, the experimental results also revealed that—under the given experimental conditions—the sample properties were significantly affected by the preparation method. In that case, there are various possible explanations for the observed behavior. For instance, chemical residues of the synthesis process, e.g. carbonates or carboxylates, are known to be very stable on cerium oxide even at temperatures as high as 500°C [74]. Such adsorbates could influence the surface defect chemistry, particularly at low oxygen vacancy concentrations, i.e. high oxygen partial pressures. Another explanation for the different experimental results could be a preferential formation of certain surfaces depending on the synthesis method. Based on the present experimental evidence, the limitation of the space charge model to fully ionized oxygen vacancies appears to be reasonable.

So far, we have concentrated on oxygen vacancies and electrons, which are the native defects in cerium oxide. In the following, the impact of interfaces on acceptor dopants will be discussed. As these defects are extrinsic in nature and hence their concentrations fixed for a given material, the effect of interfaces is essentially limited to a redistribution of ions and the concomitant indirect influence on the local defect equilibrium.

4.2. *Doped Cerium Oxide*

The segregation of foreign atoms in a host matrix is a prominent topic in materials science and specific models for ionic solids have been developed, in which the electrostatic interaction between charged solute ions and the space charge potential, the elastic energy due to size misfit of the solute ion in the host matrix, and the dipole interactions between solute-vacancy dipoles and the electric field in the space charge layers are considered as possible driving forces for segregation [75]. If we assume that no driving force for segregation of the solute exists, which would correspond to a neutral defect with perfect matching of atomic size, we expect a homogeneous distribution of the solute in the crystal lattice and the interface, Fig. 8(a). The same flat concentration profile is also considered in the Mott-Schottky model, in which equilibrium segregation of solute ions is prohibited by an activation energy barrier (leading to a non-equilibrium state). A size mismatch of the solute ion in the host matrix results in an elastic strain energy contribution to the overall enthalpy of mixing. If the size misfit can be accommodated in the structural core of an interface, the elastic strain energy h_ϵ is gained upon segregation, leading to a concentration profile as sketched in Fig. 8(b). A common approach to estimate the elastic strain energy associated with a solute atom in a matrix is to use a relationship obtained in continuum-elasticity theory [76]

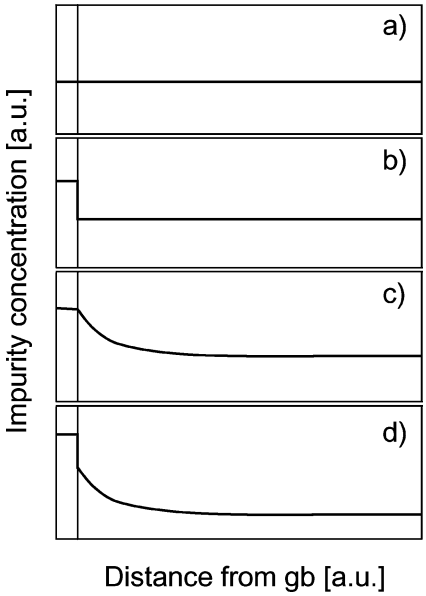

Fig. 8. Schematic concentration profiles of impurity ions perpendicular to a grain boundary for the case of (a) no segregation, (b) Langmuir-McLean type segregation, driven by size mismatch, (c) space charge segregation without size mismatch and (d) the combination of (b) and (c).

$$h_\epsilon = \frac{-24\pi K G R_m R_s (R_s - R_m)^2}{4GR_m + 3KR_s} \tag{20}$$

where R_m and R_s are the ionic radii of matrix and solute, K is the bulk modulus of the solute, and G is the shear modulus of the matrix. The two moduli

can be calculated from literature values for the elastic constants $C_{11} = 403$ GPa, $C_{12} = 105$ GPa and $C_{44} = 60$ GPa [77] and the relationships $K = (1/3)(C_{11} + 2C_{12}) = 204$ GPa and $G^{-1} = 0.6/C_{44} + 0.2/(C_{11} + C_{12}) = 86$ GPa [78, 79]. With $R_{Ce^{4+}} = 97$ pm, we obtain h_ϵ, $G_d^3+ = 0.05$ eV ($R = 105$ pm) and h_ϵ, $\mathrm{L}_\mathrm{a}^{3+} = 0.38$ eV ($R = 118$ pm).

In equilibrium, the accumulation of solute ions at the interface can be described by the Langmuir-McLean adsorption isotherm, which is given in the dilute limit by

$$\frac{\Omega}{1-\Omega} \approx x_{\mathrm{bulk}} \exp\left(-\frac{h_{\mathrm{seg}}}{k_B T}\right), \tag{21}$$

with Ω being the fraction of occupied segregation sites and $h_{\mathrm{seg}} \approx h_\epsilon$ the enthalpy of segregation.

Acceptor ions can be incorporated into the numerical model for the solution of the defect equilibrium by the assignment of a formal *energy of formation* $g^0_{A_{Ce}}$ which is treated as an adjustable variable to control the acceptor concentration. The enthalpy of solute segregation is then identical to the difference between the interface and bulk value of the formation enthalpy, i.e. $\Delta g^0_{A_{Ce}} = h_{\mathrm{seg}}$.

The segregation—driven by size mismatch—of solute ions which also carry a net charge may contribute to the formation of a space charge potential. Similar to the segregation of the native defects, the overall charge at the interface core determines the space charge potential. Also similar to the segregation of electrons, the space charge potential is still dominated by the accumulation of oxygen vacancies for large $\Delta g^0_{V_O^{\cdot\cdot}}$. Nevertheless, the solute ion distribution in equilibrium follows the electrical potential, Fig. 8(c). As a result, solute ions with negligible size mismatch may still exhibit significant segregation due to a space charge potential that is generated by the segregation of oxygen vacancies. Such a behavior may be expected for Gd-doped cerium oxide, in which the rather small size mismatch yields a segregation energy of only 0.05 eV. If size mismatch and electrostatic interaction occur simultaneously, a concentration profile as sketched in Fig. 8(d) is expected.

Any of these different situations can be analyzed using a numerical solution of the Poisson- Boltzmann equation. If space charge segregation dominates, the Gouy-Chapman model may also be alternatively used [27]. However, it is important to notice that for positive space charge potentials, the concentration of negatively charged acceptor ions close to the boundary easily exceeds values of 0.5 molar fraction so that the Boltzmann-formalism, which was derived for the dilute limit, must be replaced by Fermi-Dirac statistics. Essentially, this means that the equilibrium concentrations of defects are given by

$$x_i = X_i \frac{\delta_i}{1+\delta_i}, \tag{22}$$

with

$$\delta_i = \exp\left(-\frac{g_i^0 + z_i e_0 \Phi}{k_B T}\right). \tag{23}$$

When compared with Eq. (12), a relative error of 10% is obtained for $x_i \approx 0.11$. While the analytical Gouy-Chapman model is no longer appropriate for high defect concentrations, the Fermi-Dirac factor can be easily implemented in the numerical model.

In this chapter, the defect equilibrium of the combined thermodynamic system consisting of a crystalline phase and an individual interface was described. The specific defect chemistry of interfaces is addressed by introducing differences in the enthalpies of defect formation. In the following, the obtained results will be applied to model particles of finite size (i.e. confined in three dimensions by a closed interface) in order to introduce the grain size as a variable. Such particles are also considered to be the building units of a polycrystalline material. The effect of the interfaces becomes apparent in the grain size dependence of a given physical or chemical property.

5. Cerium Oxide Particles

5.1. Excess Oxygen Deficiency

Stereological analysis [80] shows, that the specific interface area A/V is given by

$$\frac{A}{V} = \frac{2\alpha}{\langle L \rangle_{\mathrm{area}}} \tag{24}$$

where $\langle L \rangle_{\mathrm{area}}$ is the area-weighted mean intercept length (denoted L in the following) and $\alpha = 1$ for the specific grain boundary area in polycrystalline materials while $\alpha = 2$ for the specific surface area of isolated particles. The characteristic size of the crystallites $\langle L \rangle_{\mathrm{area}}$ can be determined by applying the line

intercept method on micrographs [80] or by analysis of X-ray diffraction peak profiles [81].

The excess oxygen deficiency (or excess concentration of oxygen vacancies) was defined above in Eq. (9). A closer look at the concentration profile of oxygen vacancies perpendicular to an interface (Fig. 7) reveals, that the specific excess has two contributions with different characteristic length scales; (i) a positive excess, confined to the structural core of the interfaces with a layer thickness of 0.5–1 nm, and (ii) a negative excess, which is associated with the depletion layer and which is characterized by the screening length λ. When the size of a finite crystal is reduced to the range of $L \leq \lambda$, the depletion layers overlap so that their contribution is no longer proportional to the interface area, in other words, to the inverse grain size. As a result, the combined specific excess oxygen deficiency is no longer a constant but decreases when the grain size is reduced to values below the screening length, Fig. 9. This effect is apparently not significant in TPR or oxygen titration measurements due to the small screening length of less than 10 nm at the low oxygen partial pressures during these measurements. Nevertheless, the spatial extent of space charge layers perpendicular to the interface renders these boundary layers to three-dimensional objects which results in deviations from the characteristic scaling laws for interfaces when the grain size becomes comparable to the screening length.

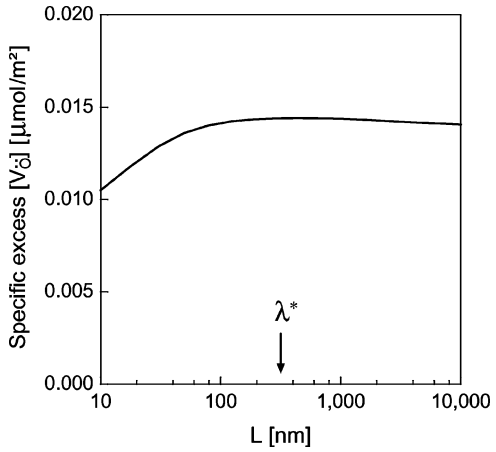

Fig. 9. Specific excess oxygen deficiency at $T = 500^\circ$C, $p_{O_2}/p^0 = 0.21$ and $\Delta\Phi = 0.58$ V as function of grain size. The drop below λ^* is caused by the enhanced depletion of overlapping space charge layers.

5.2. *Total and Bulk Acceptor Concentration*

For practical reasons, experimental studies on the grain size dependence of a physical or chemical property are typically performed on samples of a fixed composition with respect to the cations (the concentration of the volatile oxygen anions is determined by the external equilibrium). Therefore, an accumulation of solute ions at interfaces inevitably causes a decrease in the residual bulk concentration since the total concentration is constant,

$$[A'_{Ce}]_{tot} = [A'_{Ce}]_{bulk} + \frac{2\alpha}{L}\Omega \cdot \gamma^{-1/3} \qquad (25)$$

If the solute ions do not segregate ($\Omega = 0$), either because there is no driving force or because they are quenched in a flat non-equilibrium distribution, the residual bulk concentration is independent of grain size and identical to the total concentration, Fig. 10. A size mismatch between solute ions and the corresponding matrix ions results in a driving force for segregation into the interface layer as described above. In equilibrium, the residual bulk concentration can be calculated from Eqs. (21) and (25) for a given total concentration and segregation enthalpy, Fig. 10. For small grain sizes and moderate total concentrations, the amount of segregated solute is proportional to the specific interface area, i.e. $\propto L^{-1}$, and residual bulk concentrations

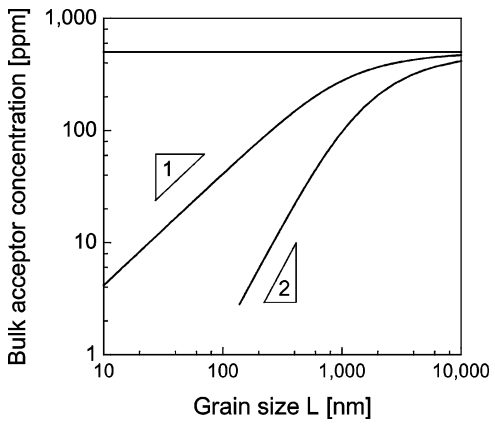

Fig. 10. Residual bulk acceptor concentration as function of the grain size of a polycrystalline material in the case of (a) no segregation, (b) Langmuir-McLean type segregation, and (c) space charge segregation ($[A'_{Ce}]_{tot} = 500$ ppm, $T = 500^\circ$C, $h_{seg} = -0.5$ eV, $\Delta\Phi = 0.58$ V).

follows a power-law dependence $[A'_{Ce}]_{bulk} \propto L$. However, if the solute ions do not exhibit a significant size mismatch but segregate into space charge layers due to electrostatic interaction, a different power-law is obtained. The origin for this difference is the correlation between the screening length and the bulk concentration of acceptor ions. When charged solute ions accumulate in space charge layers, their bulk concentration decreases which in turn increases the screening length λ leading to a further segregation of the solute. The analysis of the overall defect equilibrium revealed a power-law dependence $[A'_{Ce}]_{bulk} \propto L^2$.

Taking into account the important impact of acceptor ions to the bulk defect chemistry of cerium oxide, the various segregation mechanisms will certainly influence the grain size dependence of electrical conductivity in a characteristic way. Furthermore, electrons and oxygen vacancies as the charge carriers of the electronic and ionic current are affected by the space charge layers. In particular, electrons are accumulated while oxygen vacancies are depleted in space charge layers for $\Delta\Phi > 0$ so that the grain boundary effect on the partial conductivities should be rather different. The result of these effects will be briefly analyzed in the following chapter.

6. Effective Electrical Conductivity in Polycrystalline Cerium Oxide

The brick-layer model (BLM) is commonly used to calculate the effective electrical conductivity of a polycrystalline material. Based on the equivalent circuit of the BLM, the partial electronic and ionic conductivity of cubic cerium oxide crystals with space charge layers perpendicular and parallel to the direction of the electric field has been calculated by appropriate integration of the local conductivities. For further details, we refer to [27, 82]. However, this BLM is applicable only, if the grain size is large as compared to the screening length λ. For small grain sizes, other approaches are required. One possibility is to investigate the flat-band limit, i.e. when $L \ll \lambda$ [83].

Experimental data on the electrical conductivity of nanocrystalline cerium oxide are available in a range of grain sizes, which is neither covered by the BLM nor by the flat-band limit. In this mesoscopic range, modelling of grain size dependent conductivity requires a numerical analysis. For this purpose, methods that were developed for the simulation of semiconductor devices have been applied to mixed conductive cerium oxide. The simulation involves the solution of the Poisson-Boltzmann equation in three dimensions to obtain the equilibrium charge carrier distribution, followed by the solution of the drift-diffusion equations, which describe the non-equilibrium process of charge transport. Due to the computational expenditure, this approach is limited to small particle sizes. Further details can be found in ref. [84]. All three models could be combined to calculate the grain size dependence of the partial electrical conductivities in cerium oxide under the assumption that space charge layers exist and all defects are distributed in equilibrium. As shown in Fig. 11, a positive space charge potential results in a decreasing ionic and increasing electronic partial conductivity as the grain size is reduced into the nm regime. A comparison with the experimental results allowed to determine the value of the space charge potential as $\Delta\Phi = 0.7$ V, Fig. 11. It was further observed, that the electronic conductivity follows an L^{-3} power-law in the mesoscopic transition regime. This power-law dependence is also characteristic for the equilibrium space charge model as other exponents are expected for Langmuir-McLean-type segregation (L^{-2}) or the Mott-Schottky model with a flat acceptor concentration distribution (L^{-1}) [85].

In the given example, a transition from predominantly ionic to electronic bulk conductivity occurred at

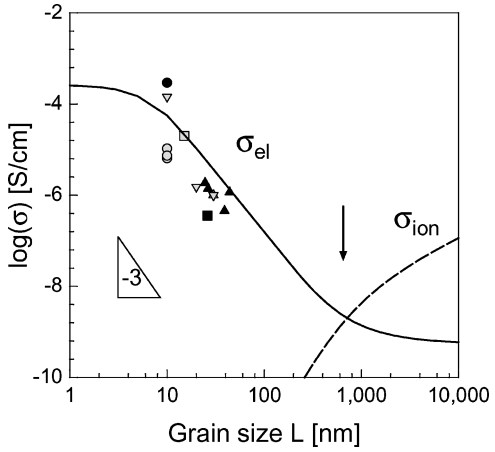

Fig. 11. Grain size dependence of electronic and ionic conductivity of cerium oxide as function of grain size. Analysis of experimental results by the space charge model revealed a space charge potential of 0.7 V [84].

a grain size of ≈90 nm. The transition from ionic to electronic conductivity was further confirmed by measurements of the grain size dependent thermopower of polycrystalline cerium oxide. The Seebeck-coefficient of a mixed conductor is determined by the partial ionic and electronic contributions, weighted by the ionic and electronic transference numbers. Furthermore, the sign of the partial Seebeck coefficient reflects the sign of the majority carrier charge which is positive for α_{ion} and negative for α_{el}. The transition from ionic to electronic conductivity is therefore evident from the change in sign of the total Seebeck coefficient, Fig. 12. The analysis of experimental results revealed a space charge potential of 0.7 ± 0.05 V.

Obviously, the electrolytic domain of cerium oxide is not only limited by acceptor concentration, temperature and oxygen partial pressure but also by grain size. A transition from the ionic to the electronic domain is expected upon reduction of grain size and the critical grain size decreases with increasing acceptor concentration. The extension of the space charge model to higher acceptor concentrations requires a numerical analysis of the Poisson-Fermi-Dirac equation. It is further desirable to find a single approach to calculate electrical conductivity for a wide range of grain sizes. Both requirements are met by the trilayer crystal model, described in Section 4.1. The layer thickness in this one-dimensional model is not limited by computing power and the application of the Fermi-Dirac factor for the calculation of high defect concentrations is readily implemented. However, it is necessary to accept the compromise associated with the transfer of the one-dimensional potential and defect concentration profiles obtained for the trilayer topology to a three-dimensional particle. A reasonable approximation is obtained, if we consider a cubic crystal that is assembled from 6 square-pyramidal fragments, which were cut out from the trilayer crystal as shown in Fig. 16. A straightforward geometrical analysis yields an approximation for the integrated acceptor concentration (Appendix 2). The calculation of partial conductivities is simplified by the fact that the ionic conductivity $\alpha_{dc,ion}$ is dominated by space charge layers perpendicular to the direction of the current, while $\alpha_{dc,el}$ is dominated by the space charge layers parallel to the direction of the current (Appendix 2).

This model allows to calculate the partial conductivities of cerium oxide as a function of temperature, oxygen partial pressure, a wide range of grain sizes and even high acceptor concentrations $[A'_{Ce}]$, Fig. 13. As expected, the bulk conductivity is dominated by the ionic contribution for a grain size of 1000 nm and $[A'_{Ce}] > 10^{-3}$ at 500°C and $p_{O_2}/p^0 = 0.21$. The ionic bulk conductivity is proportional to the total acceptor concentration for $[A'_{Ce}] \geq 10^{-3}$ but not below because the influence of space charge segregation becomes significant in this concentration range. The dc-conductivity exhibits a transition from electronic to

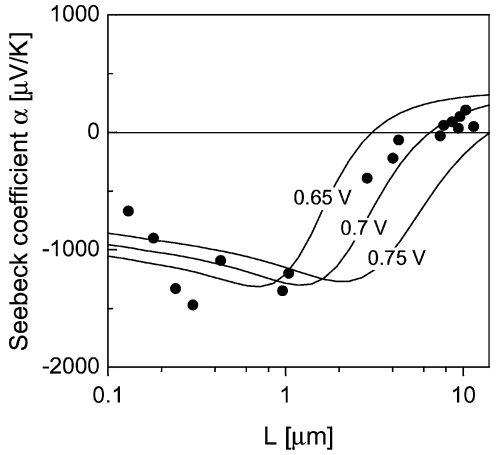

Fig. 12. Grain size dependence of the Seebeck coeficient of cerium oxide as function of grain size. Analysis of experimental results by the space charge model revealed a space charge potential of 0.7 V [34].

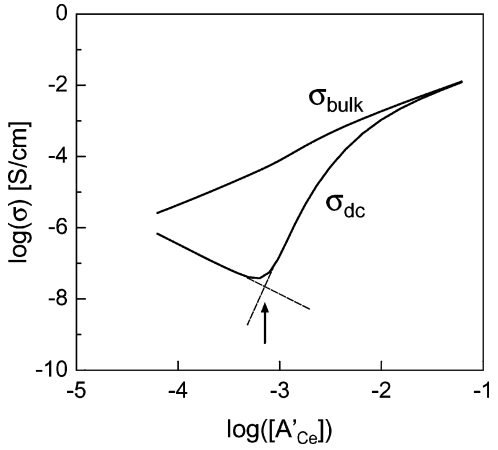

Fig. 13. Bulk and dc electrical conductivity of polycrystalline cerium oxide (1 μm grain size) at $T = 500$°C as function of acceptor concentration. The minimum in σ_{dc} as associated with the transition from predominantly electronic to ionic conductivity and defines the domain boundary.

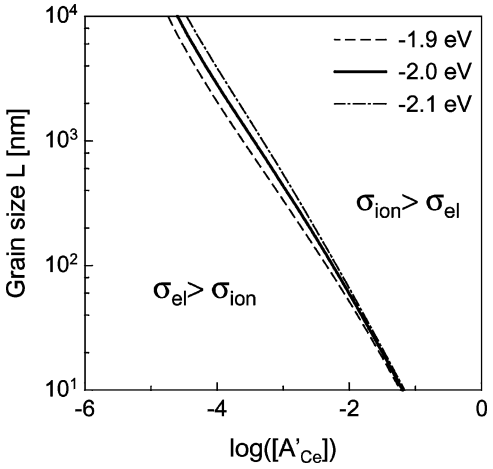

Fig. 14. Ionic/Electronic domain boundary for polycrystalline cerium oxide at $T = 500°C$ as function of grain size and acceptor concentration. The various lines correspond to different values of $\Delta g^0_{V_O^{\cdot\cdot}}$.

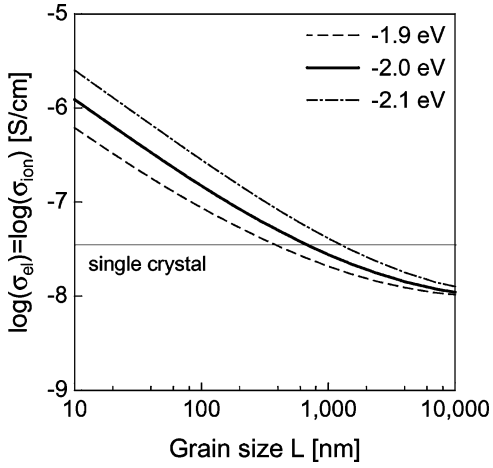

Fig. 15. Mixed ionic/electronic conductivity of polycrystalline cerium oxide at $T = 500°C$ as function of grain size. The various lines correspond to different values of $\Delta g^0_{V_O^{\cdot\cdot}}$.

ionic conductivity at $[A'_{Ce}] \approx 10^{-3}$ for the given grain size. This calculation was repeated for various grain sizes to obtain the combinations of grain size and acceptor concentration, which define the borderline of the electrolytic domain, Fig. 14. A significant grain boundary effect on the electrolytic domain is predicted. At acceptor concentrations exceeding 10%, which are typically employed in solid electrolytes, the domain boundary is crossed at a grain size of $\approx$ 20 nm. It is also interesting to estimate the mixed electronic/ionic conductivity along the borderline (defined by the condition $\alpha_{dc,ion} = \alpha_{dc,el}$), Fig. 15. The mixed conductivity increases with decreasing grain size. If compared with the corresponding value for single crystalline cerium oxide (see Fig. 1), the mixed conductivity of polycrystalline cerium oxide is smaller at large grain sizes but significantly larger in the nanometer-regime. It is also evident from Fig. 13 that the intrinsic grain boundary effect becomes smaller at large grain sizes and high acceptor concentrations. In fact, the calculated conductivities agree well with experimental results obtained for heavily doped microcrystalline cerium oxide electrolytes (see Fig. 3 in ref. [13]) except for the appearance of a characteristic maximum conductivity at $[A'_{Ce}] \approx 15\%$, which has been attributed to a correlation effect in the oxygen vacancy jump process at high vacancy concentrations [86, 87]. This particular effect is not related to the presence of interfaces and was therefore not included in the model.

Significant effects of grain size on the electrical conductivity have been reported for various nanocrystalline metals oxides, including TiO_2 [88], ZnO [89], Y-doped ZrO_2 and Yb-doped $SrCeO_3$ [90]. Whether these effects arise from changes in charge carrier mobilities (enhanced diffusion in the gb core) or charge carrier densities (which may be significantly modified by the contribution of the interface layer) needs to be evaluated in each case. The recent studies on cerium oxide demonstrated that segregation of point defects in ionic materials, which can be assumed to be a common phenomenon, should generally result in the formation of space charge layers and may have a significant effect on the properties of polycrystalline electroceramic materials. These intrinsic effects might be masked by other contributions (such as the blocking effect of an insulating phase on ionic conductivity). Furthermore, the materials engineering using space charge effects, as demonstrated by a few examples (e.g. varistor, conductivity enhancement by heterogeneous doping), could become a more general approach that has yet to be explored.

7. Summary

The defect chemistry of nanocrystalline cerium oxide was described on the basis of the equilibrium between the bulk phase and an interface layer, which are characterized by different defect formation enthalpies.

Temperature-programmed reduction and oxygen titration measurements revealed a significant excess oxygen deficiency associated with the surface of cerium oxide nanoparticles. These results suggested a reduced enthalpy of oxygen vacancy formation at the surface. In equilibrium, such a local variation in defect formation energies is the source of space charge layers. The partial pressure dependence of surface oxygen deficiency was quantitatively described by the space charge model with a difference in the enthalpy of oxygen vacancy formation of -2.3 eV . The space charge model was further applied to investigate the grain size dependence of the defect chemistry in acceptor-doped cerium oxide and to model electrical conductivity of polycrystalline cerium oxide. Numerical modelling of the defect chemistry and electrical conductivity at high acceptor concentrations was presented. This approach allowed to predict the impact of grain size in combination with dopant concentration on mixed conductivity and the electrolytic domain boundary.

Appendix A

We consider pure cerium oxide without a significant concentration of altervalent impurity ions, so that the Brouwer approximation $n = 2[V_O^{\cdot\cdot}]$ holds. The concentrations of oxygen vacancies in the bulk and at the interface (s) are gives as (see Fig. 6)

$$\frac{[V_O^{\cdot\cdot}]_{\text{bulk}}}{[O_O^x]} = \exp\left(-\frac{g^0 V_{O,\text{bulk}}^{\cdot\cdot} + 2e_0\Phi_{\text{ext}}}{k_B T}\right), \quad (26)$$

and

$$\frac{[V_O^{\cdot\cdot}]_s}{[O_O^x]} = \exp\left(-\frac{g_{V_{O,s}^{\cdot\cdot}}^0 + 2e_0\Phi_{\text{ext}} + 2e^0\Phi_{\text{int}}}{k_B T}\right), \quad (27)$$

respectively. Both equations can be combined to calculate the difference in the energy of oxygen vacancy formation,

$$\begin{aligned}\Delta g_{V_O^{\cdot\cdot}}^0 &= g_{V_{O,s}^{\cdot\cdot}}^0 - g0V_{O,\text{bulk}}^{\cdot\cdot} \\ &= -2e_0\Phi_{\text{int}} - k_B T \ln\left(\frac{[V_O^{\cdot\cdot}]_s}{[V_O^{\cdot\cdot}]_{\text{bulk}}}\right). \quad (28)\end{aligned}$$

Please notice, that Φ_{ext} cancelles in Eq. (28) so that the arbitrary choice of individual defect formation enthalpies is not significant. The oxygen vacancies at the interface provide the positive countercharge to the negative space charge Q_{sc} (in units $C \cdot m^{-2}$), which is dominated by the accumulation of electrons,

$$\begin{aligned}Q_{\text{sc}} &\approx -e_0\{n\}\Gamma = -e_0 2\lambda n \frac{-2\Theta}{1+\Theta}\Gamma \\ &\approx -e_0 2\lambda 2\Gamma[V_O^{\cdot\cdot}]_{\text{bulk}} \exp\left(\frac{\Phi_{\text{int}}}{2k_B T}\right). \quad (29)\end{aligned}$$

Here, we make use of the approximation

$$\frac{-2\Theta}{1+\Theta} \approx \exp\left(\frac{\Phi_{\text{int}}}{2k_B T}\right). \quad (30)$$

With $[V_O^{\cdot\cdot}]_s = -Q_{\text{sc}}/(2e_0\Gamma^{2/3})$ and Eq. (28), we finally obtain

$$\Delta g_{V_O^{\cdot\cdot}}^0 = -\frac{5}{2}e_0\Phi_{\text{int}} - k_B T \ln(2\lambda\Gamma^{1/3}). \quad (31)$$

Appendix B

In order to calculate the total acceptor concentration in a cubic crystal from the concentration profile, obtained for the one-dimensional problem of the trilayer crystal, we consider the cube to be composed of six square-pyramidal fragments, as shown in Fig. 16. The total

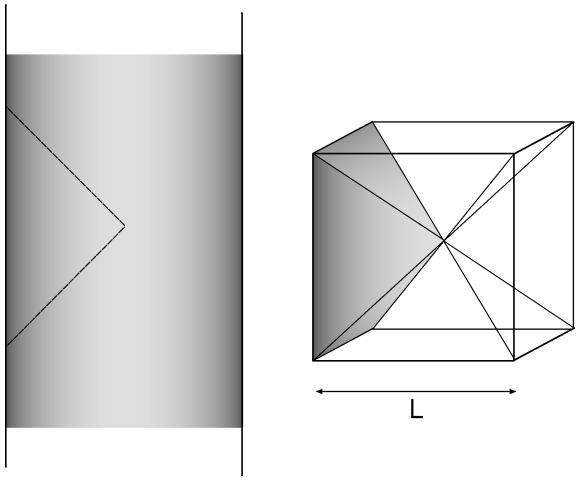

Fig. 16. For the calculation of the total acceptor concentration in a cubic crystal from the onedimensional concentration profile of the three-layer crystal, the cube is assumed to be assembled of 6 equal square-pyramidal fragments.

concentration in a cube of size L3 can be calculated from the linear concentration profile $[A'_{Ce}](\xi)$ as

$$[A'_{Ce}] = \frac{6}{L^3}\int_0^{L/2} [A'_{Ce}](\xi)\cdot(L-2\xi)^2\, d\xi. \quad (32)$$

The calculation of the ionic conductivity can be simplified by neglecting the contribution of the highly resistive space charge layers parallel to the direction of the current (a typical approximation in the BLM), resulting in

$$\sigma_{ion}^{-1} = \frac{2}{L}\int_0^{L/2} \sigma_{ion}^{-1}(\xi)\, d\xi \quad (33)$$

Similarly, the highly conductive space charge layers in series can be neglected in the calculation of the electronic conductivity, while the local conductivites are integrated over the four space charge layers in parallel,

$$\sigma_{el} = \frac{4}{L^2}\int_0^{L/2} \sigma_{el}(\xi) L\, d\xi. \quad (34)$$

Acknowledgment

The author would like to thank S. Kilassonia and R. Birringer for their valuable discussions. This work was financially supported by the German National Science Foundation (DFG, Sonderforschungsbereich 277 Grenzflächenbestimmte Materialien) and the Fonds der chemischen Industrie.

References

1. V.V. Kharton and F.M.B. Marques, *Curr. Opin. Sol. State Mater. Sci.*, **6**, 261 (2002).
2. H.L. Tuller, *Solid State Ionics*, **131**, 143 (2000).
3. J. Schoonman, *Solid State Ionics*, **135**, 5 (2000).
4. T.H. Etsel and S.N. Flengas, *Chem. Rev.*, **70**, 339 (1970).
5. H.L. Tuller and A.S. Nowick, *J. Electrochem. Soc.*, **122**, 255 (1975).
6. H.L. Tuller, in *Nonstoichiometric Oxides*, edited by T.O. Sørensen (Academic Press, New York, 1981), p. 271.
7. I. Riess, *Sol. State Ionics*, **52**, 127 (1992).
8. D.Y. Wang, D.S. Park, J. Griffith, and A.S. Nowick, *Solid State Ionics*, **2**, 95 (1981).
9. R. Gerhardt-Anderson and A.S. Nowick, *Solid State Ionics*, **5**, 547 (1981).
10. V. Butler, C.R.A. Catlow, B.E.F. Fender, and J.H. Harding, *Solid State Ionics*, **8**, 109 (1983).
11. K. Eguchi, T. Setoguchi, T. Inoue, and H. Arai, *Solid State Ionics*, **52**, 165 (1992).
12. I. Riess, M. Gödickemeier, and L.J. Gauckler, *Sol. State Ionics*, **90**, 91 (1996).
13. B.C.H. Steele, *Solid State Ionics*, **129**, 95 (2000).
14. J.A. Kilner, *Solid State Ionics*, **129**, 13 (2000).
15. R. Gerhardt and A.S. Nowick, *J. Am. Ceram. Soc.*, **69**, 641 (1986).
16. R. Gerhardt, A.S. Nowick, M.E. Mochel, and I. Dumler, *J. Am. Ceram. Soc.*, **69**, 647 (1986).
17. D.Y. Wang and A.S. Nowick, *J. Solid State Chem.*, **35**, 325 (1980).
18. M. Aoki, Y.-M. Chiang, I. Kosacki, L.J.-R. Lee, H.L. Tuller, and Y. Liu, *J. Am. Ceram. Soc.*, **79**, 1169 (1996).
19. Y.-M. Chiang, E.B. Lavik, I. Kosacki, H.L. Tuller, and J.Y. Ying, *Appl. Phys. Lett.*, **69**, 185 (1996).
20. Y.-M. Chiang, E.B. Lavik, I. Kosacki, H.L. Tuller, and J.Y. Ying, *J. Electroceramics*, **1**, 7 (1997).
21. J.H. Hwang and T.O. Mason, *Z. Phys. Chem.*, **207**, 21 (1998).
22. I. Kosacki, T. Suzuki, and H.U. Anderson, in *Solid State Ionic Devices, ECS Proceedings*, edited by E.D. Wachsman, M.-L. Liu, J.R. Akridge, and N. Yamazoe (Electrochemical Society, Pennington, 1999), Vol. 99–13, p. 190.
23. A. Tschöpe, J.Y. Ying, and H.L. Tuller, *Sensors & Actuators*, **B31**, 111 (1992).
24. A. Tschöpe, E. Sommer, and R. Birringer, *Solid State Ionics*, **139**, 255 (2001).
25. S. Kim and J. Maier, *J. Electrochem. Soc.*, **149**, J73 (2002).
26. X. Guo, W. Sigle, and J. Maier, *J. Am. Ceram. Soc.*, **86**, 77 (2003).
27. A. Tschöpe, *Solid State Ionics*, **139**, 267 (2001).
28. J. Maier, *Ber. Bunsenges. Phys. Chem.*, **88**, 1057 (1984).
29. J. Maier, *Prog. Solid State Chem.*, **23**, 171 (1995).
30. Y. Saito and J. Maier, *J. Electrochem. Soc.*, **142**, 3078 (1995).
31. P.C. McIntyre, *J. Am. Ceram. Soc.*, **83**, 1129 (2001).
32. R. Waser and R. Hagenbeck, *Acta mater.*, **48**, 797 (2000).
33. X. Guo and J. Maier, *J. Electrochem. Soc.*, **148**, E121 (2001).
34. A. Tschöpe, S. Kilassonia, B. Zapp, and R. Birringer, *Solid State Ionics*, **149**, 261 (2002).
35. A. Trovarelli, *Catalysis by Ceria and Related Materials* (Imperial College Press, London, 2002).
36. A. Bielanski and J. Haber, *Oxygen in Catalysis* (Marcel Dekker, New York, 1991).
37. H.C. Yao and Y.F. Yu Yao, *J. Catal.*, **86**, 254 (1984).
38. A.D. Logan and M. Shelef, *J. Mater. Res.*, **9**, 468 (1994).
39. M. Shelef, G.W. Graham, and R.W. McCabe, in *Catalysis by Ceria and Related Materials*, edited by A. Trovarelli (Imperial College Press, London, 2002), p. 343.
40. J. Jamnik, J. Maier, and S. Pejovnik, *Solid State Ionics*, **75**, 51 (1995).
41. H.L. Tuller and A.S. Nowick, *J. Electrochem. Soc.*, **126**, 209 (1979).
42. The value for the pre-exponential given in ref. [11] was divided by the number of CeO_2 formula units per unit volume ($2.525 \cdot 10^{22}\text{cm}^{-3}$) in order to express all defect concentrations in molar fractions.
43. O. Porat and H.L. Tuller, *J. Electroceram.*, **1**, 41 (1997).
44. D. Schneider, M. Gödickemeier, and L.J. Gauckler, *J. Electroceram.*, **1**, 165 (1997).

45. J.W. Gibbs, *Collected Works* (Yale University Press, New Haven, 1957), Vol. 1.
46. A.P. Sutton and R.W. Balluffi, *Interfaces in Crystalline Materials*, (Clarendon Press, Oxford, 1995).
47. J.W. Cahn, in *Interfacial Segregation* edited by W.C. Johnson and J.M. Blakely (ASM, Metals Park, OH, 1979), p. 3.
48. J.W. Niemantsverdriet, *Spectroscopy in Catalysis* (VCH, Weinheim, 1995).
49. P. Zimmer, A. Tschöpe, and R. Birringer, *J. Catal.*, **205**, 339 (2002).
50. S. Bernal, J.J. Calvino, G.A. Cifredo, J.M. Gatica, J.A. Perez Omil, and J.M. Pintado, *J. Chem. Soc. Faraday Trans.*, **89**, 3499 (1993).
51. M. Trudeau, A. Tschöpe, and J.Y. Ying, *Surf. Interf. Anal.*, **23**, 219 (1995).
52. A. Tschöpe and R. Birringer, *Nanostr. Mater.*, **9**, 591 (1997).
53. O. Porat, H.L. Tuller, E.B. Lavik, and Y.-M. Chiang, in *Nanophase and Nanocomposite Materials II* edited by S. Komraneni, J. Parker, and H. Wollenberger (Materials Research Society, Warrington, 1997), p. 99.
54. S. Monz, Master's thesis, Universität des Saarlandes, 2003.
55. D.M. Schaadt, Master's thesis, Universität des Saarlandes, 1997.
56. Y. Lei, Y. Ito, and N.D. Browning, *J. Am. Ceram. Soc.*, **85**, 2359 (2002).
57. Y.P. Arnaud, *Appl. Surf. Sci.*, **62**, 21 (1992).
58. J. Frenkel, *Kinetic Theory of Liquids* (Oxford University Press, New York, 1946).
59. K. Lehovec, *J. Chem. Phys.*, **21**, 1123 (1953).
60. K.L. Kliewer and J.S. Koehler, *Phys. Rev.*, **140**, 1226 (1965).
61. J.-H. Han and D.-Y. Kim, *J. Am. Ceram. Soc.*, **84**, 539 (2001).
62. J. Maier, in *Festkörper–Fehler und Funktion* (Teubner Studienbücher, Stuttgart, 2000), p. 110.
63. A.V. Chadwick and G.E. Rush, in *Nanocrystalline Metals and Oxides: Selected Properties and Applications* edited by P. Knauth and J. Schoonman (Kluwer Academic Publ., Norwell, 2002), p. 133.
64. G. Gouy, *J. Physique*, **9**, 457 (1910).
65. D.L. Chapman, *Phil. Mag.*, **25**, 475 (1913).
66. D.F. Evans and H. Wennerström, *The Colloidal Domain* (VCH Publisher, New York, 1994), p. 110.
67. D.C. Sayle, S.C. Parker, and C.R.A. Catlow, *J. Chem. Soc., Chem. Commun.*, **14**, 977, (1992).
68. D.C. Sayle, S.C. Parker, and C.R.A. Catlow, *Surf. Sci.*, **316**, 329 (1994).
69. J.C. Conesa, *Surf. Sci.*, **339**, 337 (1995).
70. G. Balducci, J. Kčaspar, P. Fornasiero, M. Graziani, and M. Saiful Islam, *J. Phys. Chem.*, **102**, 557 (1998).
71. A. Pfau and K.D. Schierbaum, *Surf. Sci.*, **321**, 71 (1994).
72. R. Birringer, M. Hoffimann, and P. Zimmer, *Z. Metallkd.*, **94**, 1052 (2003).
73. S. Kim, R. Merkle, and J. Maier, *Surf. Sci.*, **549**, 196 (2004).
74. C. Li, Y. Sakata, T. Arai, K. Domen, K. Maruya, and T. Onishi, *J. Am. Chem. Soc.*, **111**, 7683 (1989).
75. M.F. Yan, R.M. Cannon, and H.K. Bowen, *J. Appl. Phys.*, **54**, 764 (1983).
76. R.C. McCune and P. Wynblatt, *J. Am. Ceram. Soc.*, **66**, 111 (1983).
77. A. Nakajima, A. Yoshihara, and M. Ishigame, *Phys. Rev. B*, **50**, 13297 (1994).
78. W.H. Qi, M.P. Wang, and Y.C. Su, *J. Mater. Sci. Lett.*, **21**, 877 (2002).
79. H. Brooks, *Impurities and Imperfection* (American Society for Metals, Ohio, 1955), p. 1.
80. R.T. DeHoff, in *Applied Metallography* edited by G.F. Vander Voort (Van Nostrand, New York, 1986), p. 89.
81. C.E. Krill and R. Birringer, *Phil. Mag. A*, **77**, 621 (1998).
82. J. Maier, *Ber. Bunsenges. Phys. Chem.*, **90**, 26 (1986).
83. A. Tschöpe and R. Birringer, *J. Electroceramics*, **7**, 169 (2001).
84. A. Tschöpe, C. Bäuerle, and R. Birringer, *J. Appl. Phys.*, **95**, 1203 (2004).
85. A. Tschöpe, in *Solid State Ionics, MRS Proceedings* edited by P. Knauth, J.- M. Tarascon, E. Traversa, and H.L. Tuller (Materials Research Society, Warrendale, 2003), Vol. 756, p. EE4.2.
86. H. Schmalzried, *Z. Phys. Chem.*, **105**, 47 (1977).
87. A.D. Murray, G.E. Murch, and C.R.A. Catlow, *Solid State Ionics*, **18/19**, 196 (1986).
88. P. Knauth and H.L. Tuller, *J. Appl. Phys.*, **85**, 897 (1999).
89. C.-W. Nan, A. Tschöpe, S. Holten, H. Kliem, and R. Birringer, *J. Appl. Phys.*, **85**, 7735 (1999).
90. I. Kosacki and H.U. Anderson, *Ionics*, **6**, 294 (2000).